
Article:
Schuster, Christian Stefano (2020) Analytical framework for the assessment and modelling of multi-junction solar cells in the outdoors. Renewable Energy. pp. 1367-1379. ISSN 0960-1481

https://doi.org/10.1016/j.renene.2020.01.002

Analytical framework for the assessment and modelling of multi-junction solar cells in the outdoors

Christian Stefano Schuster[a]

a - Department of Physics, University of York, Heslington, York, YO10 5DD, UK

Correspondence and requests for materials should be addressed to CSS (e-mail: chriss@physics.org)

ABSTRACT

The assessment of multi-junction solar cells often relies on numerically intensive computations. Specifically, the power conversion efficiency strongly depends on the interplay between optical and electrical properties of different materials. Here, a compact and highly accurate analytical framework is proposed, facilitating the analysis of multi-junction solar cells; explicit yet simple analytical equations allow to assess the power conversion efficiency as a direct function of the cell's parameters, without restrictive assumptions. They are first used to compare the performance of the industrial state-of-the-art to multi-junction approaches. Therefore, minute data products are obtained from free satellite-services for different climatic zones over 14 years. Any variations in the operating temperature, sunshine duration, Sun's position, meteorological condition or atmospheric chemistry are thereby accounted for. Similarly, a strong site dependency is found for perovskite-on-silicon tandem cells under real-world conditions. For this, a scattering-matrix treatment is formulated based on incoherent sunlight as the relevant case. While this study gives new theoretical insights about the impact of the cell's parameters on the conversion efficiency, it also presents a powerful analytical tool for the design and assessment of more efficient solar cells in the outdoors.

Keywords: Photovoltaics; circuit model; photovoltaic modeling; silicon solar cell; multi-junction solar cells; efficiency limits

1. INTRODUCTION

Solar energy is by far the largest energy resource on Earth. Its enormous potential has kick-started great ambitions to replace conventional energy resources that were found as causes for climate and environment damaging effects [1]. However, even though solar photovoltaic (PV) has become the fastest growing renewable energy technology in the world [2], its share to the production of electricity has only been 1% in 2015. While coal and gas remain key to electricity production, solar PV still needs to prove higher conversion efficiencies at lower costs to compete with conventional technologies, see Fig. 1.

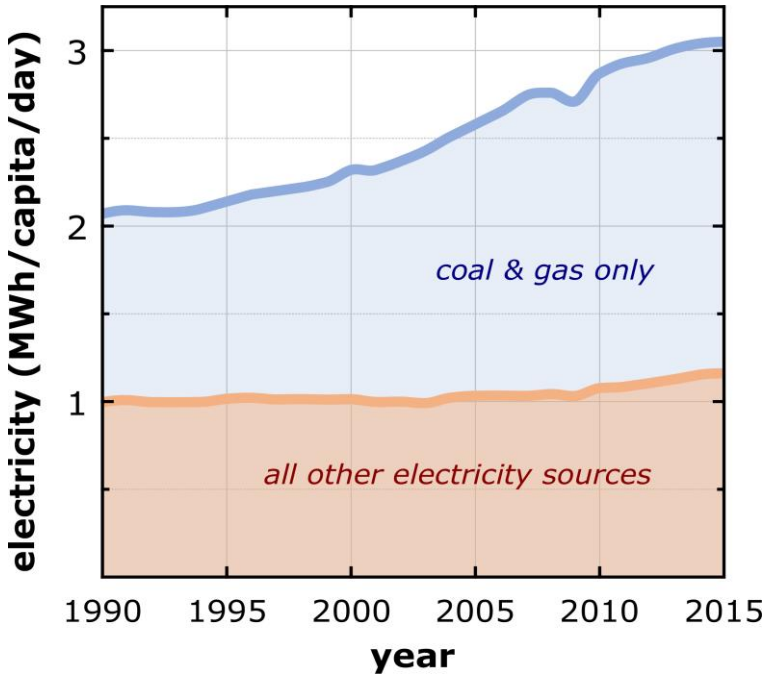

Figure 1. Daily electricity consumption per capita and production source. According to the International Energy Agency, world population grew by 40% from 1990 to 2015 whereas the demand for electricity increased by 50% in the same quarter century [3]. Key to electricity production are coal and gas compared to other electricity sources such as oil, nuclear, hydro, wind and solar PV. While coal and gas generated 52% of the electricity mix in 1990, their contribution increased to 62% in 2015. Recently, solar PV became the fastest growing renewable energy technology in the world [2], albeit its share to the production of electricity was only 1% in 2015 [3].

Today, major cost drivers of PV are linked to system components such as installation labour, racking, cabling and inverters [4]. Since most of these costs scale with the required space, a major increase in the conversion efficiency directly translates into a lower levelized cost of electricity, because the same amount of power can be produced by less area.

However, the PV industry is practically limited to a conversion efficiency of 26%, when it focuses on silicon as the only absorber material [5]. Higher efficiencies far beyond 30% were within reach, if different absorber materials are stacked on top of each other. By doing so, each layer converts a different part of the solar spectrum into electricity, thereby reducing optical as well as thermalization losses while increasing the overall power conversion efficiency [6].

Even though the multi-layer approach has been known since 1955 [7, 8], it has so far only been the selection of choice for space applications, where area is premium. Yet, the exciting achievements related to high-bandgap perovskites [9] as well as the discovery of innovative ways (e.g. mechanical stacking) to combine III/V materials with silicon [10, 11] have now launched a new development phase of multi-junction solar cell devices [12, 13, 14]. These rapid advancements could potentially have major impacts on generic terrestrial applications that require a reasonable balance between manufacturing costs and efficiency.

However, designing a novel multi-junction cell is a challenging task, because competing optical and electrical demands must be traded-off. For example, each material layer needs to be thick enough that photons in the corresponding wavelength range are absorbed but thin enough to guarantee the efficient collection of charge carriers. At the same time, each layer must deliver the maximum electrical power at the same electrical current (or voltage), which requires sophisticated and computational expensive numerical optimisation routines. For thin-films, the absorption will likely be split into multiple layers as well, which requires a demanding optical modelling approach. Finally, multi-junction cells also need a more careful evaluation to seasonal parameter changes [15], like in the temperature, daytime length, solar zenith and variations in the solar spectrum.

Here, these multiple issues are addressed with a general analytical framework. For arbitrary cell parameters, closed-form and *explicit* expressions are derived. It is also outlined how the absorption characteristics of a material layer stack can be calculated with geometric optics.

Neglecting coherent light effects is indeed without loss of generality for two reasons. Firstly, averaging Fabry-Perot interference fringes should not affect the integrated short circuit current. Secondly, the energy yield is a function of the angular-dependent incident global (hemispherical) solar spectrum throughout the day and year, so any coherent effects should again be averaged out. While seen as an acceptable simplification, non-coherence is found of greater importance in solar cell optimisations, according to Herman et al. [16]. Nevertheless, a coherent study of the materials' absorption can still be adopted.

The analytical framework is outlined in section 2 and then applied to an industrial solar panel in section 3.1 and to a perovskite-silicon tandem system in section 3.2. Since the analytical formulism enables a data-driven strategy, the examples in section 3 consider the impact of Earth's climate on the insolation. For the cities Trondheim (Norway), Paris (France), Cairo (Egypt) and Nairobi (Kenya), the **S**imple **M**odel of the **A**tmospheric **R**adiative **T**ransfer of **S**unshine *(SMARTS)* by C. Gueymard [17, 18] is used to *minutely* track the total global (hemispherical) solar spectrum on a tilted plane due to changing atmospheric and meteorological conditions. All required data series were retrieved from free-accessible satellite-product services for a period of 14 years, as described in [19]. Finally, the theoretical maximum performance of single-, double- and triple-junction solar cells are established in section 3.3 for the same high-temporal, spectral dynamics.

In brief, this paper proposes an analytical framework for the analysis of multi-junction solar cells. Whereas non-analytical approaches may heavily rely on restrictive parameter assumptions, the here presented solution allows technical studies to collapse from computational expensive endeavours to a management strategy of large datasets. The analytical framework thus empowers data-driven investigations of how weather dynamics, non-ideal device properties and the thicknesses of individual sub-cells may impact on the overall annual energy yield of solar cells.

2. METHODOLOGY

The power conversion efficiency of a (multi-junction) solar cell depends on many parameters, such as the used materials, surrounding ambient conditions and the incident solar spectrum, as indicated by Fig. 2.

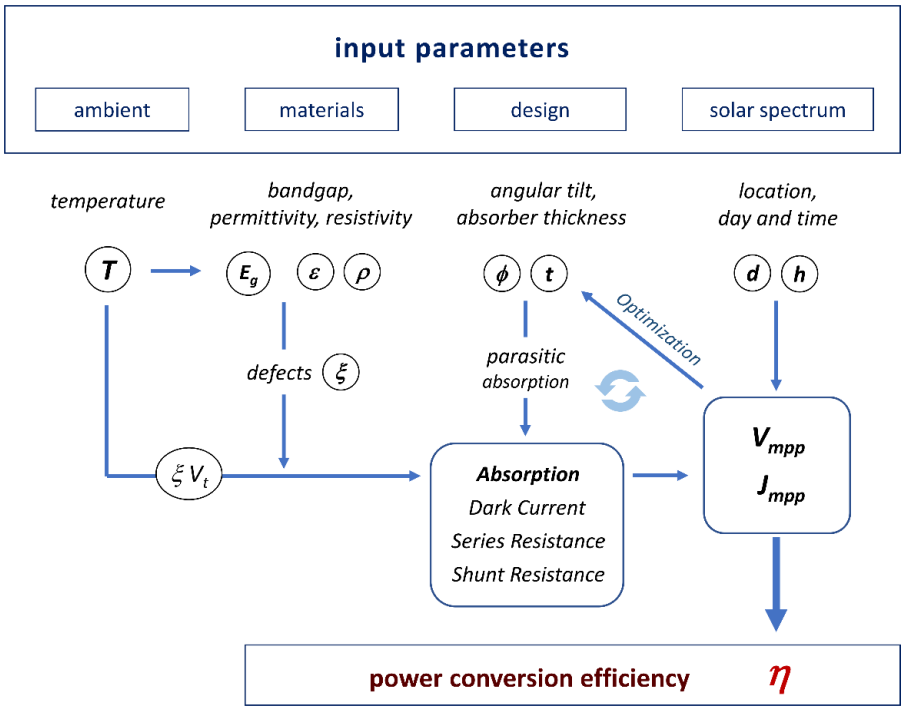

Figure 2. The conversion of solar energy into electricity is a complicated interplay of many parameters. Sophisticated optimisation routines need to carefully evaluate the optimal design parameters for a given absorber material, considering its interaction with the incident sunlight and surrounding materials. While the light induced current J_{mpp} and voltage V_{mpp} are directly linked to the incident solar spectrum, and thus are greatly affected by the position of the sun, the operating temperature influences the optical and electrical properties of a solar cell. For a multi-junction device, the key to high efficiency is a coordinated fine-tuning approach of the individual layers' optoelectronic properties to the incident solar spectrum.

For benchmarking purposes, most of the varying quantities were replaced with specific standards, set by the **A**merican **S**ociety for **T**esting and **M**aterials (ASTM), like the angle of incidence, the solar spectrum and the cell's temperature. While these simplifications led to useful design guidelines, they impede the accurate prediction of outdoor performances. For example, the recommended global solar spectrum distribution AM1.5G has already been found as unsuitable for performance prediction of terrestrial PV cells [20, 21, 22, 15]. Additionally, if a cell's electrical current is only *implicitly* given by its characteristic current-voltage relation [23], optimisation routines in a cell's design process can quickly turn complex [24]. Therefore, many research studies have either adapted a simplified cell model or used restrictive assumptions for the analysis [25] [26, 27, 28, 29, 30, 31, 32, 33, 34, 35].

In the following, *explicit* closed-form expressions of the current and voltage are derived at the maximum power point that are free of restrictive parameter assumptions (section 2.1). Secondly, a simple scattering matrix formalism is introduced to facilitate optimisation routines for the absorption characteristics of a multi-layer stack (section 2.2). Finally, it is outlined how environmental factors can be incorporated in the analysis of the harvesting efficiency (section 2.3).

2.1. THE CONVERSION EFFICIENCY OF A SOLAR CELL

Solar cells are taken as electrically equivalent to a current source J_{ph} in parallel with a diode. A series r_s and parallel resistance r_p are further added to the circuit-model to simulate series and possible shunt paths for the electrical current, respectively. If non-radiative recombination centres are modelled as defects in the diode's space charge-region by the factor ξ, with $\xi = 1$ as the defect-free case, the current-voltage characteristic of an illuminated solar cell is given by [23]:

$$J(U,J) = J_{ph} - J_o \cdot \left(\exp\left[\frac{U + r_s \cdot J}{\xi \, U_t} \right] - 1 \right) - \frac{U + r_s \cdot J}{r_p}, \qquad (1)$$

with U_t as the thermal voltage across the pn-junction of the diode. Since Shockley's diode equation does not take photon recycling into account, the reverse-saturation dark current J_o must be calculated according to the detailed balance theory outlined by Marti et al. [36].

Using the normalized quantities of Tab. 1, the current-voltage characteristic can be written in a dimensionless format

$$j(u) \;=\; q_{ph} \;-\; \frac{r}{r_p}\cdot u \;-\; \mathcal{W}(u), \tag{2}$$

via the LambertW-function LW, defined as the inverse of the function $\omega(u) = u \cdot \mathrm{e}^{u}$,

$$\mathcal{W}(u) = \mathrm{LW}\left(q_o \cdot \exp\left[q_{ph} + \frac{r}{r_s}\cdot u\right]\right). \tag{3}$$

general current	general voltage	specific resistances	dark factor	light factor
$\boldsymbol{j} = \frac{r_s J}{\xi U_t}$	$u = \frac{U}{\xi U_t}$	$\frac{r}{r_p} = \frac{r_s}{r_s + r_p}$, $\frac{r}{r_s} = \frac{r_p}{r_s + r_p}$	$q_o = \frac{r \cdot J_o}{\xi U_t}$	$q_{ph} = \frac{r \cdot (J_{ph} + J_o)}{\xi U_t}$

Table 1. The dimensionless quantities used for the analytical assessment of solar cells.

The LambertW-function LW is also known as the Omega-function, product logarithm or 'golden ratio of exponentials' [37, 38, 39, 40], and it allows to write the previous *implicitly* defined current density of Eq. 1 as an *explicit* function of the general voltage u (Eq. 2).

Solving for the voltage u_{mpp} at the maximum power point, taking $\max(j(u) \cdot u)$ leads to:

$$r_{ch} \cdot j(u_{mpp}) \;=\; r_s \cdot u_{mpp} \tag{4}$$

with the specific characteristic-resistance r_{ch} defined by

$$\frac{r_s}{r_{ch}} \;=\; \frac{\mathcal{W}(u_{mpp}) + \frac{r}{r_p}}{\mathcal{W}(u_{mpp}) + 1} \;\leq\; 1. \tag{5}$$

The following two solutions can be found for Eq. 4:

$$\mu_{max} \;=\; \kappa \cdot u_{oc}\left(\frac{r_p}{2}\right) \qquad \text{for } \mathcal{W} \ll 1, \tag{6a}$$

$$\mu_{min} \;=\; q_{ph}^{*} - \mathrm{LW}\left(q_o^{*} \cdot \mathrm{e}^{q_{ph}^{*}}\right) \qquad \text{for } \mathcal{W} \gg 1. \tag{6b}$$

147 The function u_{oc} stands for the r_s-independent open-circuit voltage, defined by Eq. 2 for $j = 0$:

148 $$u_{oc}(r_p) \;=\; q^{\diamond}_{ph} - \mathrm{LW}\left(q^{\diamond}_{o} \cdot \mathrm{e}^{q^{\diamond}_{ph}}\right), \qquad \text{with} \;\; \lim_{r_p \to \infty} u_{oc} = \ln\left(\tfrac{q_{ph}}{q_o}\right). \tag{7}$$

149 The diamond $\diamond$ or asterisk $*$ sign reflect the fact that the resistance r was either replaced with r_p or

150 $r_p / \left(1 + \frac{r_p}{2r_s}\right)$, respectively, in q_{ph} as well as q_o. The proportional constant κ describes the greatest

151 fraction of open-circuit voltage that can possibly be drawn by a load at the maximum power point:

152 $$\kappa \;=\; \lim_{r_p \to \infty} \frac{\mathrm{LW}\,\mathrm{e}^{1+u_{oc}} \;-\; 1}{\ln \mathrm{e}^{1+u_{oc}} \;-\; 1} = \frac{\mathrm{LW}\left(\frac{q_{ph}}{q_o} \cdot \mathrm{e}^{1}\right) \;-\; 1}{\ln\left(\frac{q_{ph}}{q_o} \cdot \mathrm{e}^{1}\right) \;-\; 1} \;\xrightarrow{\;q_{ph} \gg q_o\;}\; \frac{\mathrm{LW}\left(\frac{q_{ph}}{q_o}\right)}{\ln\left(\frac{q_{ph}}{q_o}\right)}. \tag{8}$$

153 One of the simplest and most popular maximum power point tracking methods is indeed based on a

154 fractional open circuit voltage technique, where κ is empirically found through extensive

155 characterizations of the PV cell and under varying meteorological conditions [41].

156 The solution of Eq. 4 is a logistic function and includes the two cases from Eq. 6:

157 $$\boldsymbol{u_{mpp}} \;=\; \boldsymbol{\mu_{max}} - \boldsymbol{m} \cdot \boldsymbol{\mu_{min}} \qquad \text{with} \;\; m(r_p) \;=\; \frac{\mu_{max} \;-\frac{u_{oc}}{2}}{u_{oc}} \;=\; \kappa \cdot \frac{u_{oc}(r_p/2)}{u_{oc}(r_p)} - \frac{1}{2}. \tag{9a}$$

158 This equation is free of any parameter assumptions and directly links the five model parameters

159 $(\xi, r_s, r_p, J_{sc}, U_{oc})$ with the cell's maximum power operating point. Therefore, it is the heart of this

160 research paper and presents the key equation of the here proposed analytical framework. Its

161 accuracy has been extensively verified on a large and diverse set of reported data, see

162 supplementary material; a gnuplot-code is also provided for the reader's own measurement sets.

163 If shunts can be neglected, hence when $1/r_p \cong 0$, only a small correction term is needed,

164 $$u_{mpp} \;=\; \kappa \cdot u_{oc}(r_p) \;-\; \left(\kappa - \tfrac{1}{2}\right) \cdot \mu_{min} \qquad \text{if} \;\; 1/r_p \cong 0, \tag{9b}$$

165 while $u_{mpp} = \mu_{max}$ in the absence of series resistances, i.e. when $r_s \cong 0$.

166 Although the two special cases in Eq. 6 were derived with assumptions on the $\mathcal{W}$-function, the

167 general solution u_{mpp} is in good agreement with the numerical results. The fill-factor FF,

168 $$FF \;=\; \frac{j_{mpp}}{q_{ph} - \;\mathrm{LW}\left(q_o \cdot \mathrm{e}^{q_{ph}}\right)} \cdot \frac{u_{mpp}}{q^{\diamond}_{ph} - \mathrm{LW}\left(q^{\diamond}_{o} \cdot \mathrm{e}^{q^{\diamond}_{ph}}\right)}, \tag{10}$$

is even indistinguishable from the numerically computed values, as shown in Fig. 3. For practical purposes, the evaluation of $j(u_{mpp})$ via Eq. 4 is not recommended, because Eq. 5 is very sensitive to small parameter changes. Therefore, j_{mpp} was calculated by inserting u_{mpp} of Eq. 9 into Eq. 2.

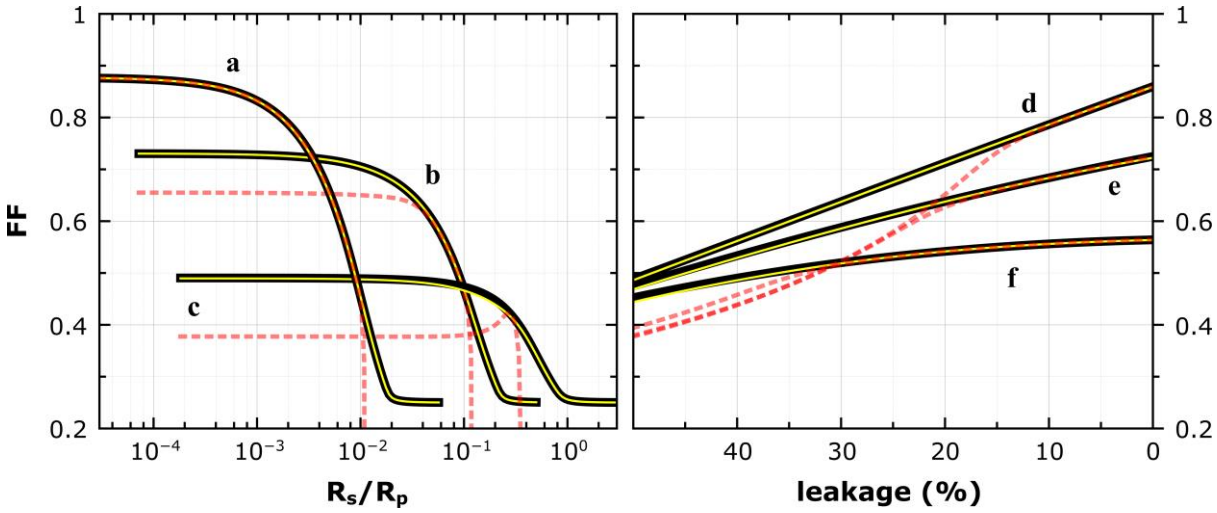

Figure 3. Excellent agreement is found between the analytical (yellow, thin solid line) and numerical (black, thick solid line) computed solutions of Eq. 4, assuming a black body spectrum at 5800 K for the Sun. The solutions proposed by Green [31] are included as red dashed lines for comparison. The left figure shows the fill factor of a GaAs solar cell (1.4 eV bandgap) at a temperature of 300 K and as a function of its series resistance r_s for three different shunt values r_p, corresponding to a=2%, b=20% and c=50% leakage current. The right figure shows the fill factor of the same GaAs cell as a function of its shunt resistance, expressed as a fraction of leakage current by $U_{oc}/(r_p J_{ph})$ for three different series resistances, d=10 Ωcm^2, e=50 Ωcm^2 and f=100 Ωcm^2. The *FF* was calculated for *ξ=1* and by inserting the analytical solution u_{mpp} from Eq. 9a into Eq. 2 and Eq. 10.

The maximum power output P of the solar cell is finally given by

$$P = J_{mpp} \cdot U_{mpp} = \frac{j(u_{mpp}) \cdot u_{mpp}}{r_s} \cdot (\xi U_t)^2 , \qquad (11)$$

hence the cell's power output can be analytically calculated via Eq. 2 and 9, for arbitrary cell parameters. Any asymptotic approximations of the LambertW-function are thereby not needed, because it is a trivial matter to incorporate the $\mathbb{LW}$-function into a non-specific software, for example, as a User Defined Function in Microsoft Excel [40], see supplementary material.

In the theoretical limit, i.e. letting $r_s \to 0$ and $r_p \to \infty$ in Eq. 11, the power output P becomes

$$P_{max} = \xi\, U_t \cdot J_{ph} \cdot \frac{\left[\mathrm{LW}\left(\frac{J_{ph}}{J_o}\cdot \mathrm{e}^1\right) - 1\right]^2}{\mathrm{LW}\left(\frac{J_{ph}}{J_o}\cdot \mathrm{e}^1\right)}, \tag{12}$$

which is known as the detailed balance limit derived by Shockley and Queisser [42, 43]. P_{max} does not increase for greater ξ values, since the reverse-saturation dark current J_o strongly depends on ξ,

$$J_o = e \cdot \int_0^\infty EQE(\lambda) \cdot \frac{2\pi\, c}{\lambda^4 \cdot \exp\left(\frac{hc/\lambda}{\xi U_t}\right)} \cdot d\lambda\,. \tag{13}$$

The photocurrent J_{ph} is defined by the solar spectrum density $GTI(\lambda)$,

$$J_{ph} = e \cdot \int_0^\infty EQE(\lambda) \cdot \frac{GTI(\lambda)}{hc/\lambda} \cdot d\lambda\,, \tag{14}$$

as a function of the wavelength λ, elementary charge e, Planck constant h and the speed of light in vacuum c. While the external quantum efficiency $EQE(\lambda)$ strongly depends on the solar elevation angle, surrounding media, layer thickness, resistivity and permittivity of the material, so does the incident solar spectrum $GTI(\lambda)$ on the geographical location – the **G**lobal **T**otal (hemispherical) **I**rradiance (GTI) is constantly changing during the day and seasons.

In the remaining part of the paper and when not otherwise stated, the dark current J_o is evaluated with $EQE = 1$ in Eq. 13 for photon energies greater than the material bandgap (zero otherwise), while for J_{ph} the layer's absorption characteristics is used, i.e. $EQE(\lambda) = A(\lambda)$ in Eq. 14.

As a final remark, Taretto et al. [29] noticed that the quantities q_{ph} and q_o are linked to the measured short-circuit current j_{sc} and open-circuit voltage u_{oc} of a solar cell. The characteristic current-voltage curve of a solar cell thus depends on only three non-directly measurable parameters, i.e. ξ, r_s and r_p. These parameters can be extracted from experimental data by standard curve-fitting procedures. For such purposes, rearranging Eq. 2 with the auxiliary quantities of Tab. 2 yields a more practical expression:

$$J(U) = \left(J_{sc} - \frac{U}{r_{tot}}\right) + \frac{1}{\alpha}\cdot\left(\alpha Q - \mathrm{LW}\left(\alpha Q \cdot e^{\alpha Q + \beta U}\right)\right) \quad \text{with } Q(\alpha, \beta, r_{tot}) = \frac{K}{\exp(k) - 1}. \tag{15}$$

The fitting parameters are α, β and r_{tot}, since they define the values of ξ, r_s and r_p. The two factors k and K are closely related to the short-circuit current J_{sc} and open-circuit voltage U_{oc} of the solar cell, whereas Q effectively plays the role of the dark-current J_o. Equation 15 is the explicit counterpart of Eq. 1. If the key goal is to find the minimum of the root mean square error, Microsoft Excel's Solver Add-in might already be able to extract the three unknown parameters.

reduced J_{sc}	reduced U_{oc}	current drop	voltage drop	total resistance
$\boldsymbol{K = J_{sc} - \frac{U_{oc}}{r_{tot}}}$	$k = u_{oc} - j_{sc}$ $= \beta U_{oc} - \alpha K$	$\alpha = \frac{r_s}{\xi U_t}$	$\beta = \frac{r_p / r_{tot}}{\xi U_t}$	$r_{tot} = r_s + r_p$

Table 2. Auxiliary quantities used for the fitting of experimental current-voltage curves. The unknown parameters are the current drop α (due to a non-negligible series resistance), the voltage drop β (due to potential shunt paths) and the total resistance r_{tot}.

2.2. ABSORPTION OF INCOHERENT SUNLIGHT

According to Herman et al. [16], tuning the absorption capability to incoherent sunlight is of greater importance for PV applications. Therefore, the scattering matrix formalism introduced by Centurioni [44, 45] is here refined for the absorption of incoherent light by a multi-layer system, such as a stack of n individual solar cells.

Let X_i be the interface matrix, describing the light reflection and transmission at the i-th interface, and L_i the layer matrix, describing the transmittance of the absorber layer i:

$$X_i = \begin{pmatrix} 1 & -R_i^- \\ R_i^+ & 1 - R_i^- - R_i^+ \end{pmatrix} \qquad L_i = \begin{pmatrix} 1/T_i^+ & 0 \\ 0 & T_i^- \end{pmatrix} \qquad \mathcal{M}_i = X_i \cdot L_i \tag{16}$$

R and T stand for the reflectance and transmittance of the incident and transmitted power, respectively. While both are wavelength, polarization and angular dependent quantities, L also depends on the total layer thickness. The lower index refers to the layer number with n as the last layer. The upper index indicates either downwards (–) or upwards (+) travelling light. For perfect anti-reflective properties ($R = 0$) or for transparent media ($T = 1$), the identity matrix is obtained.

The scattering matrix of the system $\mathcal{S}$ is now given by the product of the scattering matrices $\mathcal{M}_i$

$$\mathcal{S} = \prod_{i=1}^{n} \mathcal{M}_i \ , \qquad s = \mathcal{S}_{11} + R_{n+1}^{+} \cdot \mathcal{S}_{12} \ . \tag{17}$$

The total absorption of light in layer i can now be determined via the absorption matrix $\mathcal{A}_i$:

$$\mathcal{A}_i = \prod_{j=1}^{i} \left(1 - R_j^{+}\right) \cdot (L_i - \mathbb{1}) \cdot \mathcal{Q}_i \qquad \text{with } \mathcal{Q}_i = \frac{1}{s} \prod_{j=i+1}^{n} \mathcal{M}_j \text{ and } \mathcal{M}_{n+1} = \mathbb{1} \ . \tag{18}$$

Computing the energy flux Φ_i in layer i

$$\Phi_i = \begin{pmatrix} \phi_i^{+} \\ \phi_i^{-} \end{pmatrix} = \varphi_i \cdot \left[\mathcal{A}_i \cdot \begin{pmatrix} 1 \\ R_{n+1}^{+} \end{pmatrix} \right] \qquad \text{with } \varphi_i = \frac{\mathrm{Re}(\gamma_i)}{\prod_{j=1}^{i} \mathrm{Re}\left(\frac{\gamma_j}{\gamma_{j-1}}\right)} \tag{19}$$

finally allows to calculate the total absorption in layer i

$$A_i = \phi_i^{+} - \phi_i^{-} \ . \tag{20}$$

The γ-factor in Eq. 19 is defined for layer i by

$$\gamma_i = \frac{N_i^{(*)}}{N_0} \cdot \frac{\cos \vartheta_i}{\cos \vartheta_0} \tag{21}$$

and describes the undergoing effects of the energy flux in the direction normal to the i-th interface for s-polarized light (N_i) or p-polarized light (N_i^{*}). The first factor reflects the respective change in velocity, expressed by the complex indices of refraction N; the second term accounts for variations in the area cross-section, expressed by the incident and refracted angle ϑ_0 and ϑ_i, respectively.

2.3. AMBIENTAL AND ATMOSPHERIC EFFECTS

Since solar cells are encapsulated in PV modules, their operating temperature T is in general higher than the ambient temperature T_{amb}. This is especially the case in the afternoon, when more heat is radiated out by Earth's surface, once the local insolation has passed its peak value. However, higher temperatures can lead to significant increases in J_0 (see Eq. 13) and in turn to a reduction in the power conversion efficiency.

A simple and widely used way to estimate the operating cell temperature is given by [46]

$$T \ = \ T_{amb} + \ (NOCT - 20) \cdot \frac{P_{sun}}{800}, \tag{22}$$

where P_{sun} stands for the total incident solar irradiance in W/m^2 and *NOCT* for the **N**ominal **O**perating **C**ell **T**emperature, which is typically around 48 °C for silicon. The $NOCT$ is defined as the mean solar cell junction temperature within an open-rack mounted module in a standard reference environment: tilt angle at normal incidence to the direct solar beam at local solar noon; total irradiance of 800 W/m^2; ambient temperature of 20 °C; wind speed of 1 m/s and nil electrical load. It is an important parameter in module characterisation, since it is a reference of how the module will work when operating in real conditions.

Although records for P_{sun} are widely available, the irradiance is a spectrally integrated quantity and, as such, cannot resolve the impact of spectral variations on a solar energy technology. For multi-junction solar cells, the actual solar spectrum is therefore needed. But while the sunshine received by a terrestrial solar panel continuously changes due to Earth's rotation and revolution, the solar spectrum also depends on the chemical composition and meteorological condition of the atmosphere – both being subject to fluctuations on a minutely time scale. In order to account for these dynamics, *minutely* time series of historical, global (hemispherical) solar spectra between 2004 and 2018 were reconstructed from multiple satellite-retrieved datasets via the open-source program SMARTS [17, 18]; the method is in detail described in [19]. This sequence of spectra was then used as the solar resource data *GTI(λ)* in the integral of Eq. 14.

3. RESULTS & DISCUSSION

The analytical formalism of Section 2 allows to calculate the maximum power of a solar cell for arbitrary model parameters. As such, the incident solar spectrum could be treated as a variable quantity now. The following three examples are based on this idea and highlight how one can study the impact of a highly-variable solar spectrum on the potential energy yield.

By minutely tracking any variations in the Sun's position, sunshine duration, meteorological condition and atmospheric chemistry, a series of historical, global (hemispherical) solar spectra at one-minute

intervals were retrieved from 2004 to 2018 for the four different climatic zones on Earth, as in [19], represented by Trondheim (Norway), Paris (France), Cairo (Egypt) and Nairobi (Kenya). All here considered examples use these sequences of spectra as the solar resource data *GTI(λ)* in the integral of Eq. 14. The management and analysis of the large datasets is performed by the software Maple 2017 from Maplesoft on the **Y**ork **A**dvanced **R**esearch **C**omputing **C**luster (YARCC).

First, since Eq. 9 and Eq. 11 analytically link the maximum output power to the incident solar spectrum for arbitrary electrical parameters, a typical industrial cell is considered in Section 3.1. The model parameters are listed in Tab. 3 and were extracted from SunPower datasheets; its optical response has been reported as the *EQE* of a SunPower's Maxeon™ II solar cell. Furthermore, to clarify whether changes in the solar spectrum or ambient temperature have the greatest effect on the annual energy yield, their influences are separately assessed.

Second, choosing the optimal thickness combination of different absorber materials is often a challenging task. However, since Eq. 12 and Eq. 20 now directly link the maximum output power of a multi-junction solar cell to the individual layers' thicknesses, the analytically approach simplifies the analysis with material functions and is here applied to a perovskite-silicon tandem device in Section 3.2.

Finally, the theoretical (detailed balance) limit for terrestrial solar cells is derived in Section 3.3 by using a sequence of multi-year solar spectra instead of a standard solar spectrum [47].

3.1. PV PERFORMANCE OF CURRENT'S INDUSTRIAL STATE-OF-THE-ART

The annual energy yield of a typical industrial solar cell is derived for the following cases:

1. The cell is kept at a constant temperature.
2. The cell and the surrounding ambient have the same temperature.
3. The cell experiences the elevated temperature of a module according to Eq. 22.
4. As case 2, but the absorption is 100% for photons beyond the silicon bandgap and 0% otherwise.
5. As case 3, but the absorption is 100% for photons beyond the silicon bandgap and 0% otherwise.

These differentiations allow to distinguish the impact of local temperatures from variations in the solar spectrum, established by the site-specific meteorological and atmospheric dynamics.

The cell's parameters are listed in Tab. 3, whereas the front reflection R_1 is assumed to follow the correction factor chosen by Ramirez [48] for the cases 1-3,

$$R_1(\vartheta_0) = 0.1 \cdot \left(\frac{1}{\cos \vartheta_0} - 1\right), \tag{23}$$

with the angle of incidence ϑ_0, and $R_1 = 0$ otherwise.

Figure 4 summarizes the outcomes and shows how the performance of a typical industrial solar cell depends on the geographical location. While the cell at Cairo may not work as efficient as at Trondheim, Cairo's insolation level is still twice as much compared to Trondheim and, therefore, enables a far higher energy yield. The comparison shows, that if solar cells can absorb more sunlight at the same temperature, the efficiency gains will exceed those achieved by passive cooling methods alone. Industrial solar panels thus have the potential to increase efficiency levels by 4% in absolute by combining radiative cooling methods [49] with absorption enhancement schemes [50, 51, 52, 53, 54, 55, 56]. Consequently, while large area silicon cells are approaching their practical Shockley-Queisser-limit of 26% in the lab/fab [5], more R&D efforts are needed to boost their performances to the same level in the outdoors.

J_{sc}	V_{oc}	η	ξ	J_o	r_s	r_p	*NOCT*
41.66 mA/cm²	0.68 V	22.1 %	1.02	193 fA/cm²	1.14 Ω.cm²	4.87 kΩ.cm²	48 °C

Table 3. Representative parameter set for industrial silicon solar cells. The dark current J_o, non-ideality factor ξ and specific series r_s and shunt r_p resistances were extracted from the IV data-curve of a SunPower® E20/333 solar panel at standard test conditions, whereas the short-circuit current J_{sc}, open-circuit voltage V_{oc} and power conversion efficiency η were derived from the AM 1.5G solar spectrum [57], using the external quantum efficiency (*EQE*) of a SunPower's Maxeon™ II solar cell. All quantities are normalized to the average cell area of 170 cm², i.e. to the total SunPower panel area (1.63 m²) divided by the number of interconnected Maxeon cells (96). In addition, a more typical value of 48 °C is assumed for the nominal operating cell temperature *NOCT* instead of SunPower's certified 45 °C.

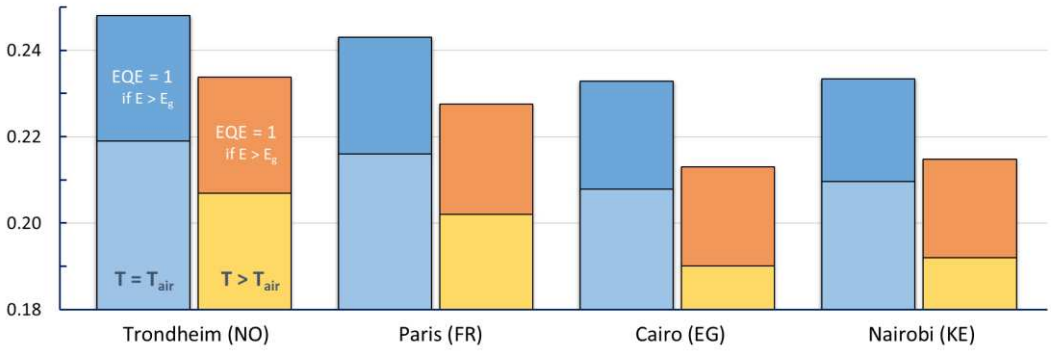

Figure 4. The performance of a typical industrial silicon solar cell at four climatic-distinctive cities. The overall conversion efficiency (ordinate) is defined by the ratio of the total energy yield to the total insolation received between February 2004 and February 2018. Using a dynamic solar spectrum with a 1 nm spectral and 1 min temporal resolution, the latitude-tilted solar cell of Tab. 3 is modelled to follow either the actual ambient temperature *($T=T_{air}$)* or elevated temperature *($T>T_{air}$)* according to Eq. 22. If the absorption were unity up to the absorption edge, the absolute efficiency gain would be greater at Trondheim (+2.7 %) than at Nairobi (+2.3 %). In contrast, passive cooling techniques have a greater effect at Cairo than at Trondheim, translating into an absolute efficiency gain of +1.8 % and +1.2 %, respectively. When combining the two effects, cooling and unity quantum yield, the absolute gain becomes almost independent of the location (+4.1 ± 0.1 %). Additional increases in the overall conversion efficiency are then only possible by reducing series resistances, shunt paths, non-radiative recombination centres and electrical noise. For comparison, the power conversion efficiency is 0.221 under standard test conditions.

3.2. THE PEROVSKITE-SILICON TANDEM CELL

One way of improving the overall efficiency of a silicon solar cell is the inclusion of a top absorber layer with a higher energy bandgap than silicon. If the high energy photons are all absorbed in the top layer, thermalization losses would be greatly reduced, because they are caused by the blue part of the solar spectrum in silicon. In principal, a silicon-based tandem cell then operates at a lower temperature.

Yamaguchi et al. reviewed the progresses and challenges for integrating silicon with other materials [58]. The authors quote perovskite materials as a promising candidate for this endeavour – like many others [15, 59, 60]. In fact, despite their extraordinary short history as PV material [59], rapid developments already enabled 27% efficient silicon-perovskite tandem cells [60, 61], exceeding the 26.7% efficiency of the current world-record single-junction silicon solar cell [62]. However, the efficiency testing of some high-performance perovskite-based cells is often completed under the inert atmosphere in a glove box.

Nevertheless, Hoerantner and Snaith [63] modelled the silicon-perovskite tandem performance under the most typical outdoor conditions. Since the authors used a constant silicon substrate thickness of 3.5 mm for the yield optimisation, instead of a usual wafer thickness between 100 and 300 µm, their approach neglects the optical interplay between the perovskite and silicon material. Therefore, the scattering-matrix formalism for incoherent sunlight (see Section 2.2) is here applied to establish the theoretical upper limit of a silicon-perovskite tandem cell under actual solar spectra. The reflection between air and the perovskite's front interface thereby follows Ramirez correction factor, according to Eq. 23, whereas the back interface of the substrate is assumed to be 100% reflective to imitate the presence of a high-reflective mirror. The reflectances of all other interfaces are given by Fresnel's energy equations, i.e. not by the ratio of the waves' electric (or magnetic) field amplitudes but their absolute squares.

3.2.1 THE MATERIAL FUNCTION OF A MAPI LAYER

A $CH_3NH_3PbI_3$ (MAPI) layer with an energy bandgap of 1.55 eV is placed onto a crystalline silicon substrate. MAPI is currently one of the most widespread perovskite compositions found in the literature [64, 65, 66, 67, 68, 69, 70, 71, 72, 73] [74, 75, 76, 77], yet its material function shows significant variations, see Fig. 5. Here, the data by Jiang et al. [71] are chosen, because the authors characterised the film properties in detail over a wide wavelength range (from 300 nm to 2500 nm) by combining the measurement results of variable angle spectroscopic ellipsometry, spectrophotometry and atomic force microscopy.

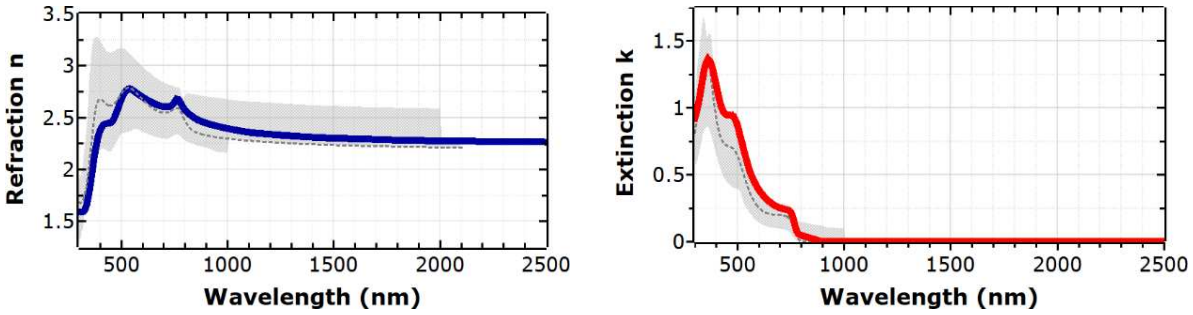

Figure 5. The refractive index (left) and extinction coefficient (right) of planar $CH_3NH_3PbI_3$ (MAPI) layers. The solid line refers to the data published by Jiang et al. [71], used in this study, whereas the thin dashed line refers to the data by Löper et al. [68]. The results are based on a film thickness of 200 nm and 300 nm, respectively. Although both studies analysed the MAPI layer over a wide range of wavelengths via multiple techniques, the coefficients do not overlap. Generally, large differences can be found in the literature [64, 65, 66, 67, 68, 69, 70, 71, 72] for the dielectric function of MAPI, as highlighted by the grey shaded area.

3.2.2 THE TEMPERATURE DEPENDENCE OF A MAPI-SI TANDEM CELL

While a MAPI-Si tandem cell could potentially operate at a lower temperature than a silicon solar cell, the tandem cell is still considered to experience the same elevated temperature of a typical silicon-only device, according to Eq. 22. This particular choice is motivated by both the lack of underlying data available [78], and the many ongoing challenges related to the outdoor deployment of perovskite modules [79]. For example, Dupre et al. [80] showed that a “thermal benefit” strongly

depends on the global heat transfer mechanisms between the module and its (outdoor) surrounding. Yet, the multiple interfaces of a perovskite solar cell stack can lead to mechanical failure during temperature cycling [81]. Cai et al. [82] also noticed a 30% efficiency drop by an increased contact resistance when going from 1 cm^2 cells to 25 cm^2 modules, whereas Stoichkov et al. [83] observed a rapid degradation of perovskite mini-modules under outdoor conditions, caused by breaches of the edge sealant. Finally, while most of the research has only been done on solution-processed perovskites, a spin-coating deposition technique is seen as incompatible with high-volume manufacturing methods. Therefore, perovskite layers ultimately employed in the field might show different physical properties as those currently associated with MAPI. Reference [79] gives a comprehensive discussion about the major impediment to highly efficient, stable and low-cost perovskites.

3.2.3 THE LAYER THICKNESS OF MAPI FOR SI-BASED TANDEM CELLS

Figure 6 compares the thickness dependence of the MAPI layer for different silicon substrates. Firstly, the annual energy yield scales with the substrate thickness, because the two cells are series-connected. The photo-generated current in the silicon layer limits the total electrical current of the tandem device. Secondly, the MAPI thickness scales with the location's latitude. As the solar irradiance decreases in the visible part of the spectrum, so does the photocurrent of the MAPI film. However, the near-infrared part of the spectrum is less affected by latitudinal changes, such that a thicker MAPI layer better mitigates current mismatches with the silicon bottom cell at higher latitudes. Thirdly, the application of a MAPI layer always reduces the overall performance, if series connected [76], hence the highest yield is obtained by a single-junction silicon solar cell. The bandgap combination of MAPI and silicon is the reason for this observed setback, as shown in section 3.3: In theory, if all photons with energy above the bandgap were to contribute to the individual cells' electrical currents (ideal scenario), shifting the bandgap of the top cell from 1.55 eV to 1.70 eV could dramatically increase the overall conversion efficiency of a silicon-based tandem cell

from ca. 30% to over 40%; in practice, however, the higher the bandgap of the top cell, the more photons are transmitted to the silicon substrate, and thus the thicker the top layer must become to mitigate the effects of an increased photocurrent of the bottom cell.

Since parasitic influences by the absorber and other important cell materials have so far been ignored, making thick – i.e. more than 1 µm thick layers [63] – and high-quality crystallized perovskites might become crucial for the application of high-bandgap perovskites in silicon-based tandem cells.

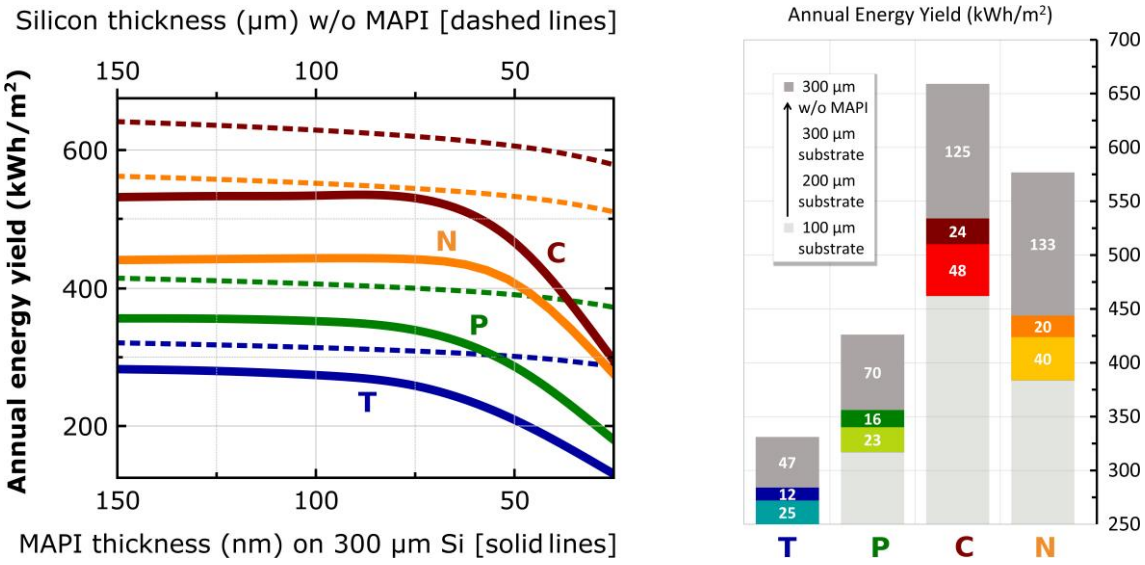

Figure 6. Annual energy yields of latitude-tilted solar cells. Neither shunts nor series resistances and only radiative recombinations were assumed for the analysis. The left figure compares the outdoor performance of silicon solar cells [dashed lines] to perovskite-silicon tandem devices [solid lines] at Trondheim (T), Paris (P), Cairo (C) and Nairobi (N). Apparently, the deposition of a MAPI layer on crystalline silicon reduces the energy yield of a silicon solar cell. The coloured bars in the right figure quantify the increases in annual energy yield when going from a 100 µm to a 300 µm thick silicon substrate for a 200 nm (T), 150 nm (P), 100 nm (C) and 75 nm (N) MAPI coating, and after its removal (dark grey).

As one of the lead movers in this technology, Snaith's group already made a transition from MAPI to mixed cation and mixed anion materials [84], such as $Cs_x(MA_{0.17}FA_{0.83})_{1-x}Pb(I_{0.83}Br_{0.17})_3$. The bandgap of this triple-cation perovskite could potentially be increased beyond 1.65 eV by raising the Cs content *x* [85]. Yang et al. [86] thoroughly discuss the strategies and challenges for achieving high-bandgap perovskite materials for multi-junction solar cells.

3.3. LIMITING EFFICIENCIES OF TERRESTRIAL SOLAR CELLS UNDER DYNAMIC SOLAR SPECTRA

For general terrestrial applications, the harvesting or overall efficiency of a solar cell is defined by the ratio of the useful electricity produced and the total insolation received over the same time window. Following the method set out in [19], a 14-year time series of minutely terrestrial global (hemispherical) solar spectra was reconstructed to establish the limiting efficiencies of latitude-tilted (ideal) solar cells at four distinct climatic zones. The commonly definition of ideal solar cells is adopted by the following qualities:

1. no reflection losses for all angles of incidence,
2. 100% absorption for photons above the energy bandgap (0% otherwise),
3. only direct bandgap transitions,
4. only radiative charge-carrier recombinations,
5. no electrical shunts nor series resistance effects,
6. a vanishing absorber thickness,
7. operating at ambient temperature.

The limiting efficiencies of a single, tandem and triple energy bandgap cell are shown in Fig. 7, 8 and 9, respectively. While the optimum bandgap shows a weak site-dependency, using real material properties and thickness values could severely reduce the limiting efficiencies, as discussed in section 3.2.3.

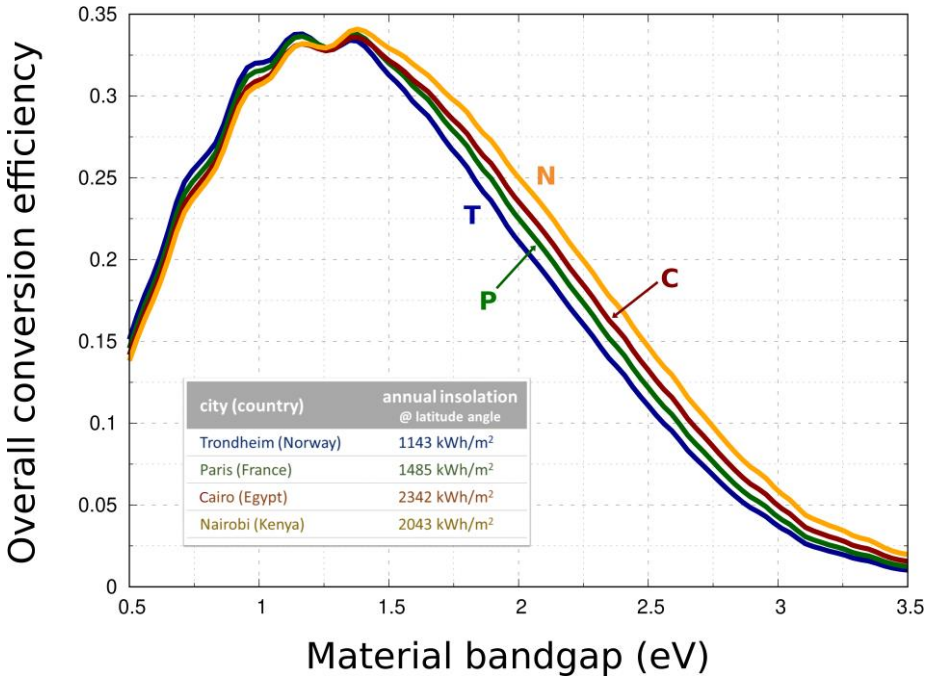

447

448 **Figure 7.** Limiting conversion efficiency of latitude-tilted, idealised single-junction cells as a function of the
449 material bandgap. For every minute, the produced electricity and the received insolation were derived from
450 satellite data series between 2004 and 2018 for the locations Trondheim (T), Paris (P), Cairo (C) and Nairobi (N),
451 following the method set out in [19]. After integration, the ratio of the total generated electricity and total
452 received solar insolation defines the overall conversion efficiency.

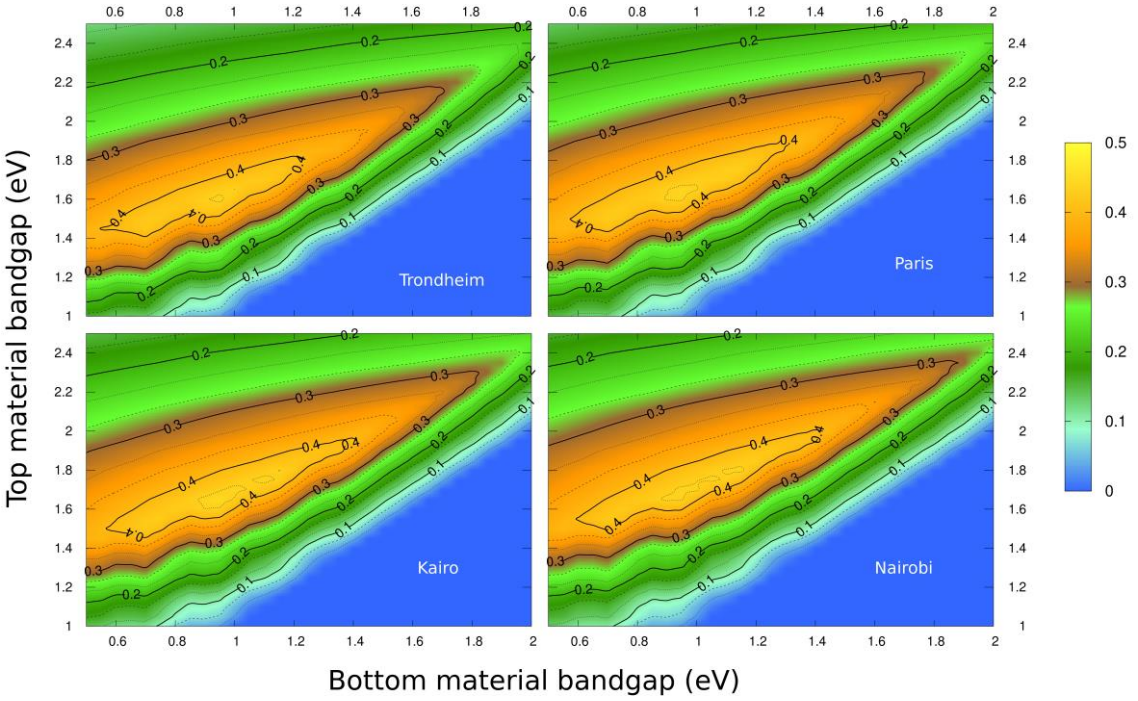

453

454 **Figure 8.** Limiting conversion efficiency of latitude-tilted, idealised double-junction solar cells as a function of

455 the top and bottom material bandgap. For every minute, the produced electricity and the received insolation

456 were derived from satellite data series between 2004 and 2018, following the method set out in [19]. After

457 integration, the ratio of the total generated electricity and total received solar insolation defines the overall

458 conversion efficiency.

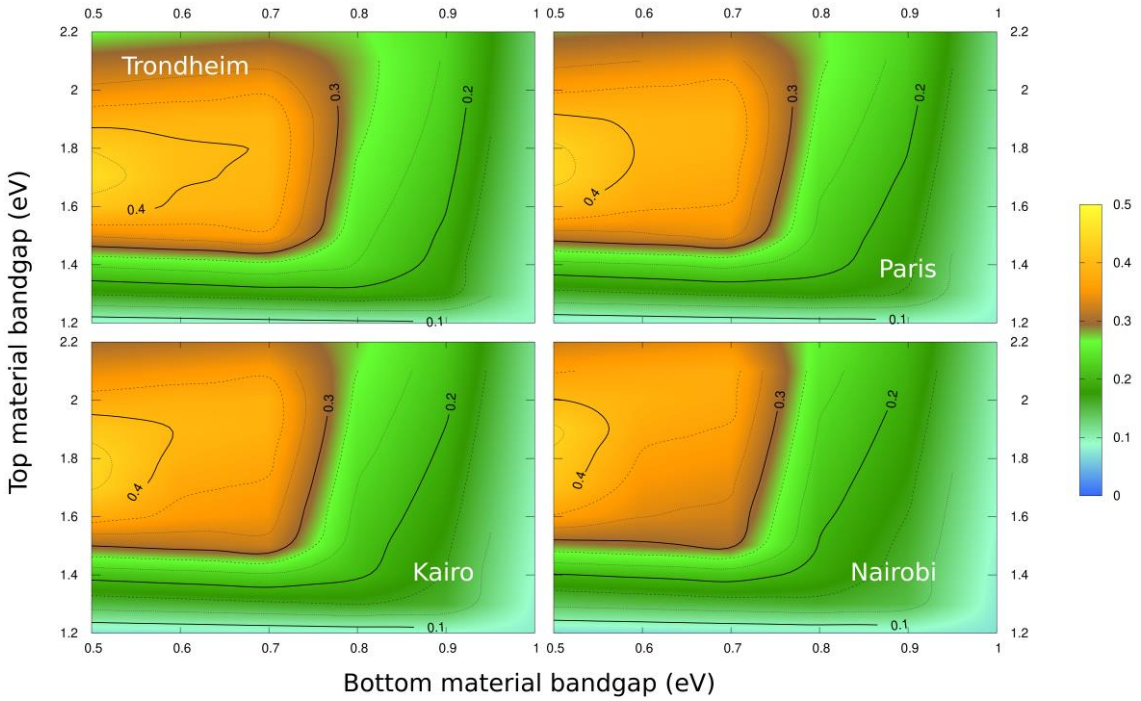

Figure 9. Limiting conversion efficiency of latitude-tilted, idealised triple-junction solar cells as a function of the top and bottom material bandgap. The middle cell is assumed to be made of a bandgap of 1.1 eV, representative for silicon. For every minute, the produced electricity and the received insolation were derived from satellite data series between 2004 and 2018, following the method set out in [19]. After integration, the ratio of the total generated electricity and total received solar insolation defines the overall conversion efficiency.

4. SUMMARY AND CONCLUSIONS

Driven by the need to replace conventional but environmentally damaging electricity resources, such as coal and gas, solar PV emerged as the fastest growing renewable energy technology in the world. Its enormous potential, however, may not be unlocked if solar cells are based on only one absorber material. Therefore, multi-junction technologies are increasingly appealing as a pathway to go, due to the rapid developments of high-bandgap perovskites and the progresses in combining III/V materials with silicon. Multi-junction solar cells, however, require a more careful evaluation, because they are more susceptible to spectral variations [15].

Here, the impact of weather/climate effects on the energy yield of solar cells is rigorously analysed by modelling the incident spectrum at a high spectral and temporal resolution, i.e. at 1 nm wavelength intervals and at 1 min time steps, over a long-time window (14 years) and for the main climatic zones. Therefore, a scattering-matrix treatment is formulated based on incoherent sunlight, as it is seen as the more relevant case for photovoltaics. Secondly, while the modelling of solar cells has previously relied on numerical solutions for the maximum electrical power, often at the cost of computational demanding operations or numerical stability issues, a framework is here proposed that is suitable for the analytical assessment of multi-junction solar cells. For arbitrary cell parameters, closed-form and *explicit* expressions are derived to facilitate both design optimisation routines and the accurate modelling of PV outdoor performances with observational datasets.

The current industrial state-of-the-art, its limiting potential and the ongoing developments are thus reviewed from a different perspective. In contrast to previous studies that have only focused on the (spectrally integrated) irradiance, multiple satellite-product services are used to retrieve long-time series of historical, global (hemispherical) solar spectra. As major issues relevant to the deployment of solar cells can thereby be quantified, key differences between the performance in the lab and under the effects of a dynamic solar spectrum are apparent. For example, if passive cooling and advanced light management techniques were combined, a 26% harvesting efficiency is found as a more realistic limit for conventional silicon cells, but which is almost 10% in absolute lower than the theoretical radiative limit (34%) derived from idealised conditions.

In case of perovskite-silicon tandem cells, the perovskite's bandgap will need to be carefully tuned to a desirable thick silicon substrate, though its layer thickness and material quality would also need to be traded off: Since the bandgap of $CH_3NH_3PbI_3$ is too low (1.55 eV), depositing a MAPI film onto a 300 µm thick silicon substrate reduces the harvesting efficiency of a silicon-only device (29%) by 4% (Trondheim) to 7% (Nairobi) in absolute. In contrast, efficiencies higher than 40% are more likely obtained by a high-crystalline but thick (> 1 µm) perovskite layer with bandgap of 1.70 eV. Alternatively, if the silicon were used as the middle cell of a triple-junction approach, the bandgap

sensitivity issue becomes relaxed and would make a thin MAPI layer (< 200 nm) more acceptable as top cell. Fig. 10 summarizes the differences, challenges and opportunities for multi-junction solar cells in different climatic zones.

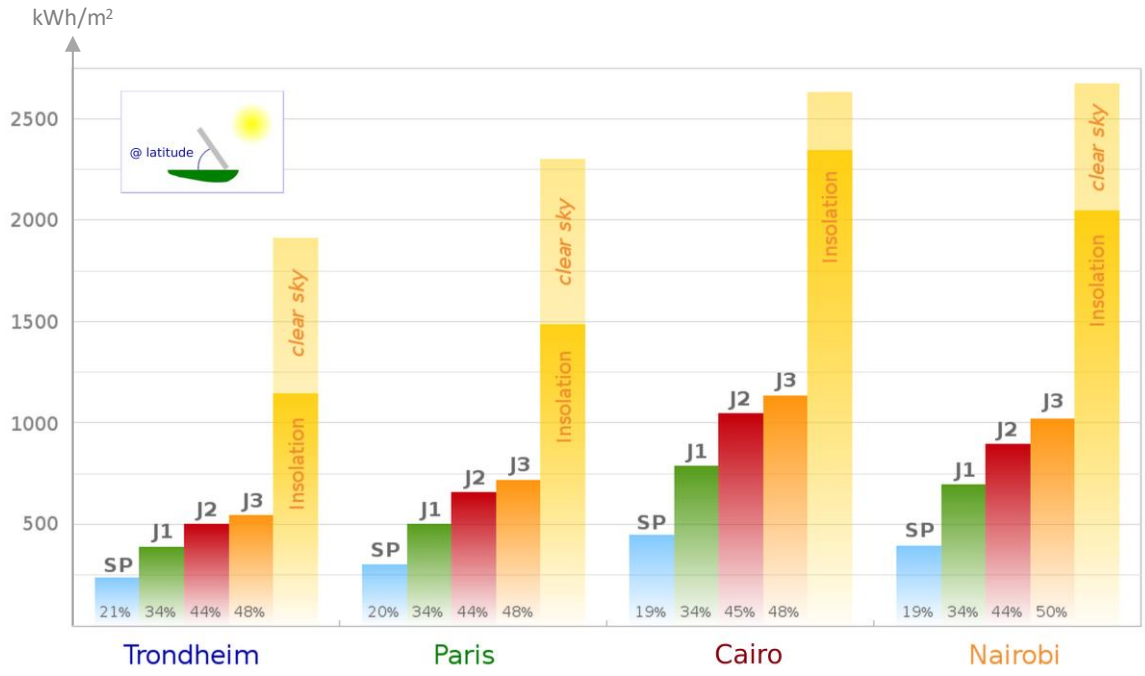

Figure 10. Comparison of an industrial standard solar panel (SP) to the theoretical maximum annual energy yield of idealised multi-junctions in four distinct climatic zones; J1, J2 and J3 indicate the number of junctions. The insolation is taken as 100% for the overall efficiency, shown at the bottom of the bars. The modelled clear-sky insolation is included as a light-coloured bar to the insolation, for comparison. All surfaces are latitude-tilted, facing toward the Equator. While the harvesting efficiencies are almost site-independent, the energy yield is sensitive to the geographical location and all-sky conditions. For example, a single-junction cell at Cairo can produce more electricity than a multi-junction cell at Trondheim or Paris. While Cairo and Nairobi have approximately the same clear-sky conditions, Nairobi still receives less sunshine than Cairo due to a more frequent cloud formation and higher air pollution level.

Since the active area is assumed to be free of any debris in this study, the effect of snow cover periods and the impact of ice, shadings or dirt along with any induced material degradations are left out. The potential energy yield should also be judged by the AC-DC conversion losses over the lifetime of the PV system, but is neglected here. Finally, the temperature will likely not be uniformly distributed in multi-junction cells. So future work would need to consider the impact of thermal gradients as well as the temperature dependency of the dielectric function.

In summary, an analytical solution is derived for the maximum electrical power of a solar cell. Since the general solution (Eq. 9a) is free of restrictive parameter assumptions, technical studies now could collapse from computational expensive endeavours to simple data management strategies. Here, three data-driven examples are indeed based on this approach, as they break free from solving a complicated or transcendental equation numerically. Consequently, the application of the framework may become a crucial factor in the response analysis of solar modules, because it effectively enables to model the behaviour of all its interconnected sub-cells analytically. In conclusion, this paper not only indicates critical aspects for the deployment of multi-junction technologies in the outdoors, but it does also give new theoretical insights about the impact of the cell's parameters on the conversion efficiency and thus presents a powerful analytical tool for the design and assessment of more efficient solar cells.

5. ACKNOWLEDGEMENTS

This research did not receive any specific grant from funding agencies in the public, commercial, or not-for-profit sectors. Thanks are given to Andrea Canino, Alberto Jimenez, Stefan Kremer, Kezheng Li, Manuel Mendes, Claudio Padilha, Dario Rapisarda, Mark Scullion and Brian Smith for their thorough and helpful critiques. The author wants to thank the Institute of Physics for the carer and beneficiary fund, but also to Sara Castillo Avila for her patience, encouragements and continuous support over the past two years, in particular.

6. ADDITIONAL INFORMATION

Competing interests: The author declares no competing financial and non-financial interests in relation to the work described.

7. REFERENCES

[1] V. Masson-Delmotte, P. Zhai, H. O. Pörtner, D. Roberts, J. Skea, P. R. Shukla, A. Pirani, W. Moufouma-Okia, C. Péan, R. Pidcock, S. Connors, J. B. R. Matthews, Y. Chen, X. Zhou, M. I. Gomis, E. Lonnoy, T. Maycock, M. Tignor and T. Waterfield, Eds."IPCC Special Report on the impacts of global warming of 1.5°C," *World Meteorological Organization,* 2018.

[2] IEA, "Renewables 2017: Analysis and Forecasts to 2022," 2017.

[3] "Based on IEA data from the yearly electricity and heat data service © OECD/IEA 2015," Licence: www.iea.org/t&c; as modified by Christian Schuster, [Online]. Available: https://www.iea.org/classicstats/.

[4] IRENA, "The Power to Change: Solar and Wind Cost Reduction Potential to 2025," 2016.

[5] D. D. Smith, P. Cousins, S. Westerberg, R. D. Jesus-Tabajonda, G. Aniero and Y.-C. Shen, "Toward the Practical Limits of Silicon Solar Cells," *IEEE Journal of Photovoltaics,* vol. 4, no. 6, 2014.

[6] D. J. Friedman, "Progress and challenges for next-generation high-efficiency multijunction solar cells," *Current Opinion in Solid State and Materials Science,* vol. 14, p. 131–138, 2010.

[7] E. Jackson, "Areas for improvement of the semiconductor solar energy converter," *Trans. Conference on the Use of Solar Energy, Tucson, Arizona (1955), University of Arizona Press,* vol. 5, p. 122–126, 1958.

[8] E. Jackson, "Solar energy converter". U.S. Patent 2949498, 16 Aug. 1960.

[9] M. A. Green and A. Ho-Baillie, "Perovskite Solar Cells: The Birth of a New Era in Photovoltaics," *ACS Energy Lett.,* vol. 2, pp. 822-830, 2017.

[10] K. Tanabe, K. Watanabe and Y. Arakawa, "III-V/Si hybrid photonic devices by direct fusion bonding," *Scientific Reports,* vol. 2, no. 349, 2012.

[11] D.-M. Geum, M.-S. Park, J. Y. Lim, H.-D. Yang, J. D. Song, C. Z. Kim, E. Yoon, S. Kim and W. J. Choi, "Ultra-high-throughput Production of III-V/Si Wafer for Electronic and Photonic Applications," *Scientific Reports,* vol. 6, no. 20610, 2016.

[12] I. Mathews, D. O'Mahony, B. Corbett and A. P. Morrison, "Theoretical performance of multi-junction solar cells combining III-V and Si materials," *Optics Express,* vol. 20, no. S5, pp. A754-A764, 2012.

[13] F. Dimroth, M. Grave, P. Beutel, U. Fiedeler, C. Karcher, T. N. O. E. Tibbits, G. Siefer, M. Schachtner, A. Wekkeli, A. W. K. R. Bett, M. Piccin, N. Blanc, C. Drazek, E. Guiot, B. Ghyselen, T. Salvetat, A. Tauzin, T. Signamarcheix, A. Dobrich, T. Hannappel and K. Schwarzburg, "Wafer bonded four-junction GaInP/GaAs//GaInAsP/GaInAs concentrator solar cells with 44.7% efficiency," *Prog. Photovolt: Res. Appl.,* vol. 22, no. 3, pp. 1062-7995, 2014.

[14] R. Cariou, J. Benick, F. Feldmann, O. Höhn, H. Hauser, P. Beutel, N. Razek, M. Wimplinger, B. Bläsi, D. Lackner, M. Hermle, G. Siefer, S. W. Glunz, A. W. Bett and F. Dimroth, "III–V-on-silicon solar cells reaching 33% photoconversion efficiency in two-terminal configuration," *Nature Energy,* vol. 3, p. 326–333, 2018.

[15] F. T. Si, O. Isabella and M. Zeman, "Too Many Junctions? A Case Study of Multijunction Thin-Film Silicon Solar Cells," *Adv. Sustainable Syst.,* vol. 1, no. 1700077, 2017.

[16] A. Herman, M. Sarrazin and O. Deparis, "The fundamental problem of treating light incoherence in photovoltaics and its practical consequences," *New Journal of Physics,* vol. 16, no. 013022, 2014.

[17] C. Gueymard, "Parameterized Transmittance Model for Direct Beam and Circumsolar Spectral Irradiance," *Solar Energy,* vol. 71, no. 5, pp. 325-346, 2001.

[18] C. Gueymard, "SMARTS, A Simple Model of the Atmospheric Radiative Transfer of Sunshine: Algorithms and Performance Assessment," *Professional Paper FSEC-PF-270-95. Florida Solar Energy Center, 1679 Clearlake Road, Cocoa, FL 32922,* 1995.

[19] C. Schuster, "The quest for the optimum angular-tilt of terrestrial solar panels or their angle-resolved annual insolation," *Renewable Energy,* vol. submitted, 2019.

[20] T. Zdanowicz, T. Rodziewicz and M. Zabkowska-Waclawek, "Theoretical analysis of the optimum energy band gap of semiconductors for fabrication of solar cells for applications in higher latitudes locations," *Solar Energy Materials & Solar Cells,* vol. 87, p. 757–769, 2005.

[21] A. E. Ghitas, "Studying the effect of spectral variations intensity of the incident solar radiation on the Si solar cells performance," *NRIAG Journal of Astronomy and Geophysics,* vol. 1, no. 2, pp. 165-171, 2012.

[22] E. Gouvêa, P. Sobrinho and T. Souza, "Spectral Response of Polycrystalline Silicon Photovoltaic Cells under Real-Use Conditions," *Energies,* vol. 10, no. 8, p. 1178, 2017.

[23] M. B. Prince, "Silicon Solar Energy Converters," *Journal of Applied Physics,* vol. 26, pp. 534-540, 1955.

[24] A. T. Vicente, P. J. Wojcik, M. J. Mendes, H. Águas, E. Fortunato and R. Martins, "A statistics modeling approach for the optimization of thin film photovoltaic devices," *Solar Energy,* vol. 144, pp. 232-243, 2017.

[25] M. A. Green, "Solar Cell Fill Factors: general graph and empirical expressions," *Solid-State Electronics,* vol. 24, no. 8, pp. 788-789, 1981.

[26] A. Jain and A. Kapoor, "Exact analytical solutions of the parameters of real solar cells using Lambert W-function," *Solar Energy Materials & Solar Cells,* vol. 81, p. 269–277, 2004.

[27] H. Bayhan and A. S. Kavasoglu, "Exact Analytical Solution of the Diode Ideality Factor of a pn Junction Device Using Lambert W-function Model," *Turk J Phys,* vol. 31, pp. 7-10, 2007.

[28] C. Zhang, J. Zhang, Y. Hao, Z. Lin and C. Zhu, “A simple and efficient solar cell parameter extraction method from a single current-voltage curve,” *J. Appl. Phys.,* vol. 110, no. 064504, 2011.

[29] K. Taretto, M. Soldera and M. Troviano, “Accurate explicit equations for the fill factor of real solar cells - Applications to thin-film solar cells,” *Prog. Photovolt: Res. Appl. ,* vol. 21, p. 1489–1498, 2013.

[30] J. Cubas, S. Pindado and C. De Manuel, “Explicit Expressions for Solar Panel Equivalent Circuit Parameters Based on Analytical Formulation and the Lambert W-Function,” *Energies,* vol. 7, pp. 4098-4115, 2014.

[31] M. A. Green, “Accurate expressions for solar cell fill factors including series and shunt resistances,” *Appl. Phys. Lett.,* vol. 108, no. 081111, 2016.

[32] J. Cubas, S. Pindado and F. Sorribes-Palmer, “Analytical Calculation of Photovoltaic Systems Maximum Power Point (MPP) Based on the Operation Point,” *Appl. Sci. ,* vol. 7, no. 870, 2017.

[33] B. A. Ikyo, A. Johnson and F. Gbaorun, “Analytical Solution to Nonlinear Photovoltaic Diode Equation,” *Mind Sourcing,* vol. 2017, no. 20170512, 2017.

[34] S. Pindado and J. Cubas, “Simple mathematical approach to solar cell/panel behavior based on datasheet information,” *Renewable Energy,* vol. 103, pp. 729-738, 2017.

[35] S. Pindado, J. Cubas, E. Roibás-Millán, F. Bugallo-Siegel and F. Sorribes-Palmer, “Assessment of Explicit Models for Different Photovoltaic Technologies,” *Energies,* vol. 11, no. 1353, 2018.

[36] A. Marti, J. L. Balenzategui and R. F. Reyna, “Photon recycling and Shockley’s diode equation,” *J. Appl. Phys.,* vol. 82, no. 8, pp. 4067-4075, 1997.

[37] R. M. Corless, G. H. Gonnet, D. E. G. Hare, D. J. Jeffrey and D. E. Knuth, “On the LambertW function,” *Adv Comput Math,* vol. 5, no. 1, p. 329–359, 1996.

[38] B. Hayes, “Why W?,” *American Scientist,* vol. 93, no. 2, pp. 104-108, 2005.

[39] P. B. Brito, F. Fabião and A. Staubyn, “Euler, Lambert, and the LambertW-function today,” *Mathematical Scientist ,* vol. 33, no. 2, pp. 127-133, 2008.

[40] S. Disney and R. Warburton, “On the Lambert W function: EOQ applications and pedagogical considerations,” *Pre-prints of the 16th International Working Seminar of Production Economics, Innsbruck, Austria,* vol. 1, pp. 129-140, 2010.

[41] M. T. Penella and M. Gasulla, “A Simple and Efficient MPPT Method for Low-Power PV Cells,” *Int. J. of Photoenergy,* vol. 2014, no. 153428, 2014.

[42] W. Shockley and H. J. Queisser, “Detailed Balance Limit of Efficiency of pn Junction Solar Cells,” *J. Appl. Phys.,* vol. 32, no. 3, pp. 510-519, 1961.

[43] W. Marx, “The Shockley-Queisser paper – A notable example of a scientific sleeping beauty,” *Ann. Phys.,* vol. 526, no. 5-6, p. A41–A45, 2014.

[44] E. Centurioni, “Generalized matrix method for calculation of internal light energy flux in mixed coherent and incoherent multilayers,” *Applied Optics,* vol. 44, no. 35, pp. 7532-7539, 2005.

[45] E. Centurioni, “A GPL optical simulation program for mixed coherent/incoherent multilayer systems,” *available at www.bo.imm.cnr.it/~centurio/optical.html,* 2018.

[46] M. A. Garcia and J. Balenzategui, “Estimation ofphotovoltaic module yearly temperature and performance based on Nominal Operation Cell Temperature calculations,” *Renewable Energy,* vol. 29, p. 1997–2010, 2004.

[47] C. H. Henry, “Limiting efficiencies of ideal single and multiple energy gap terrestrial solar cells,” *J. Appl. Phys.,* vol. 51, no. 4494, pp. 4494-4500, 1980.

[48] I. L. Ramirez, “Operating correction factor of PV system,” *Master thesis, University of Gävle,* 2017.

[49] L. Zhu, A. Raman, K. X. Wang, M. A. Anoma and S. Fan, “Radiative cooling of solar cells,” *Optica,* vol. 1, no. 1, 2014.

[50] O. Isabella, R. Vismara, D. Linssen, K. X. Wang, S. Fan and M. Zeman, “Advanced light trapping scheme in decoupled front and rear textured thin-film silicon solar cells,” *Solar Energy,* vol. 162, p. 344–356, 2018.

[51] Z. Yuan, C. Schuster, A. Marconi, A. Anopchenko, G. Pucker and L. Pavesi, “Photovoltaic properties of Si nanostructure-based thin films fabricated on quartz,” *E-MRS Spring meeting, Strasbourg, France,* 2010.

[52] C. S. Schuster, P. Kowalczewski, E. R. Martins, M. Patrini, M. G. Scullion, M. Liscidini, L. Lewis, C. Reardon, L. C. Andreani and T. F. Krauss, “Dual gratings for enhanced light trapping in thin-film solar cells by a layer-transfer technique,” *Optics Express,* vol. 21, no. S3, pp. A433-A438, 2013.

[53] C. S. Schuster, A. Bozzola, L. C. Andreani and T. F. Krauss, “How to assess light trapping structures versus a Lambertian Scatterer for solar cells ?,” *Optics Express,* vol. 22, no. S2, pp. A542-A551, 2014.

[54] M. J. Mendes, A. Araújo, A. Vicente, H. Águas, I. Ferreira, E. Fortunato and R. Martins, “Design ofoptimized wave-optical spheroidal nanostructures for photonic-enhanced solar cells,” *Nano Energy,* vol. 26, p. 286–296, 2016.

[55] L. C. Andreani, A. Bozzola, P. Kowalczewski, M. Liscidini and L. Redorici, “Silicon solar cells: toward the efficiency limits,” *Advances in Physics: X,* vol. 4, no. 1, 1548305, 2018.

[56] O. Sanchez-Sobrado, M. J. Mendes, S. Haque, T. Mateus, A. Araujo, H. Aguas, E. Fortunatoa and R. Martins, “Colloidal-lithographed TiO2 photonic nanostructures for solar cell light trapping,” *J. Mater. Chem. C,* vol. 5, no. 27, pp. 6852-6861, 2017.

[57] *NREL, Reference Solar Spectral Irradiance: Air Mass 1.5 (2018), https://rredc.nrel.gov/solar//spectra/am1.5/.*

[58] M. Yamaguchi, K.-H. Lee, K. Araki and N. Kojima, “A review of recent progress in heterogeneous silicon tandem solar cells,” *J. Phys. D: Appl. Phys.,* vol. 51, no. 133002, 2018.

[59] J. Werner, B. Niesen and C. Ballif, “Perovskite/Silicon Tandem Solar Cells: Marriage of Convenience or True Love Story? – An Overview,” *Adv. Mater. Interfaces,* vol. 5, no. 1700731, 2018.

[60] C. O. R. Quiroz, Y. Shen, M. Salvador, K. Forberich, N. Schrenker, G. D. Spyropoulos, T. Heumüller, B. Wilkinson, T. Kirchartz, E. Spiecker, P. J. Verlinden, X. Zhang, M. A. Green, A. Ho-Baillie and C. J. Brabec, “Balancing electrical and optical losses for efficient 4-terminal Si–perovskite solar cells with solution processed percolation electrodes,” *J. Mater. Chem. A,* no. 8, pp. 3583-3592, 2018.

[61] T. Sherahilo, “Oxford PV sets world record for perovskite solar cell,” Oxford PV, 25 June 2018. [Online]. Available: https://www.oxfordpv.com/news/oxford-pv-sets-world-record-perovskite-solar-cell. [Accessed December 2018].

[62] M. A. Green, Y. Hishikawa, E. D. Dunlop, D. H. Levi, J. Hohl-Ebinger and A. W. Ho-Baillie, “Solar cell efficiency tables (version 52),” *Prog Photovolt Res Appl.,* vol. 26, p. 427–436, 2018.

[63] M. T. Hörantner and H. J. Snaith, “Predicting and optimising the energy yield of perovskite-on-silicon tandem solar cells under real world conditions,” *Energy Environ. Sci.,* vol. 10, pp. 1983-1993, 2017.

[64] G. Xing, N. Mathews, S. S. Lim, N. Yantara, X. Liu, S. Dharani, M. Grätzel, S. Mhaisalkar and T. C. Sum, “Low-temperature solution-processed wavelength-tunable perovskites for lasing,” *Nature Materials,* vol. 13, p. 476–480, 2014.

[65] X. Ziang, L. Shifeng, Q. Laixiang, P. Shuping, W. Wei, Y. Yu, Y. Li, C. Zhijian, W. Shufeng, D. Honglin, Y. Minghui and G. G. Qin, “Refractive index and extinction coefficient of CH3NH3PbI3 studied by spectroscopic ellipsometry,” *Optical Materials Express,* vol. 5, no. 1, pp. 29-43, 2014.

[66] Y. Jiang, M. A. Green, R. Sheng and A. Ho-Baillie, “Optical modelling data for room temperature optical properties of organic–inorganic lead halide perovskites,” *Data in Brief,* vol. 3, pp. 201-208, 2015.

[67] Y. Jiang, M. A. Green, R. Sheng and A. Ho-Baillie, “Room temperature optical properties of organic–inorganic lead halide perovskites,” *Solar Energy Materials & Solar Cells,* vol. 137, pp. 253-257, 2015.

[68] P. Löper, M. Stuckelberger, B. Niesen, J. Werner, M. Filipič, S.-J. Moon, J.-H. Yum, M. Topič, S. D. Wolf and C. Ballif, “Complex Refractive Index Spectra of CH3NH3PbI3 Perovskite Thin Films Determined by Spectroscopic Ellipsometry and Spectrophotometry,” *J. Phys. Chem. Lett.,* vol. 6, p. 66−71, 2015.

[69] L. J. Phillips, A. M. Rashed, R. E. Treharne, J. Kay, P. Yates, I. Z. Mitrovic, A. Weerakkody, S. Hall and K. Durose, “Dispersion relation data for methylammonium lead triiodide perovskite deposited on a (100) silicon wafer using a two-step vapour-phase reaction process,” *Data in Brief,* vol. 5, pp. 926-928, 2015.

[70] S. Foster and S. John, “Light-trapping design for thin-film silicon-perovskite tandem solar cells,” *J. Appl. Phys.,* vol. 120, no. 103103, 2016.

[71] Y. Jiang, A. M. Soufiani, A. Gentle, F. Huang, A. Ho-Baillie and M. A. Green, “Temperature dependent optical properties of CH3NH3PbI3 perovskite by spectroscopic ellipsometry,” *Appl. Phys. Lett.,* vol. 108, no. 061905, 2016.

[72] J. A. Guerra, A. Tejada, L. Korte, L. Kegelmann, J. A. Töfflinger, S. Albrecht, B. Rech and R. Weingärtner, “Determination of the complex refractive index and optical bandgap of CH3NH3PbI3 thin films,” *J. Appl. Phys.,* vol. 121, no. 173104, 2017.

[73] C.-W. Chen, S.-Y. Hsiao, C.-Y. Chen, H.-W. Kang, Z.-Y. Huang and H.-W. Lin, “Optical properties of organometal halide perovskite thin films and general device structure design rules for perovskite single and tandem solar cells,” *J. Mater. Chem. A,* vol. 3, p. 9152–9159, 2015.

[74] M. Filipič, P. Löper, B. Niesen, S. D. Wolf, J. Krč, C. Ballif and M. Topič, “CH3NH3PbI3 perovskite / silicon tandem solar cells: characterization based optical simulations,” *Optics Express,* vol. 23, no. 7, pp. A263-A278, 2015.

[75] W. E. I. Sha, X. Ren, L. Chen and W. C. H. Choy, “The efficiency limit of CH3NH3PbI3 perovskite solar cells,” *Appl. Phys. Lett.,* vol. 106, no. 221104, 2015.

[76] M. H. Futscher and B. Ehrler, “Modeling the Performance Limitations and Prospects of Perovskite/Si Tandem Solar Cells under Realistic Operating Conditions,” *ACS Energy Lett.,* vol. 2, p. 2089−2095, 2017.

[77] D. Liu, M. K. Gangishetty and T. L. Kelly, “Effect of CH3NH3PbI3 thickness on device efficiency in planar heterojunction perovskite solar cells,” *J. Mater. Chem. A,* vol. 2, p. 19873–19881, 2014.

[78] S. Castro-Hermosa, S. K. Yadav, L. Vesce, A. Guidobaldi, A. Reale, A. Di Carlo and T. M. Brown, “Stability issues pertaining large area perovskite and dye-sensitized solar cells and modules,” *J. Phys. D: Appl. Phys.,* vol. 50, no. 033001, 2016.

[79] Y. Zhang, H. Zhang, X. Zhang, L. Wei, B. Zhang, Y. Sun, G. Hai and Y. Li, “Major Impediment to Highly Efficient, Stable and Low-Cost Perovskite Solar Cells,” *Metals,* vol. 8, no. 964, 2018.

[80] O. Dupré, B. Niesen, S. D. Wolf and C. Ballif, “Field Performance versus Standard Test Condition Efficiency of Tandem Solar Cells and the Singular Case of Perovskites/Silicon Devices,” *J. Phys. Chem. Lett.,* vol. 9, p. 446−458, 2018.

[81] R. Cheacharoen, N. Rolston, D. Harwood, K. A. Bush, R. H. Dauskardt and M. D. McGehee, “Design and understanding of encapsulated perovskite solar cells to withstand temperature cycling,” *Energy Environ. Sci.,* vol. 11, no. 1, pp. 144-150, 2018.

[82] L. Cai, L. Liang, J. Wu, B. Ding, L. Gao and B. Fan, “Large area perovskite solar cell module,” *J. Semicond.,* vol. 38, no. 014006, 2017.

[83] V. Stoichkov, N. Bristow, J. Troughton, F. D. Rossi, T. M. Watson and J. Kettle, “Outdoor performance monitoring of perovskite solar cell mini-modules: Diurnal performance,

observance of reversible degradation and variation with climatic performance," *Solar Energy,* vol. 170, pp. 549-556, 2018.

[84] H. J. Snaith and S. Lilliu, "The Path to Perovskite on Silicon PV," *Scientific Video Protocols,* vol. 1, no. 1, pp. 1--8, 2018.

[85] P. Brenner, T. Glöckler, D. Rueda-Delgado, T. Abzieher, M. Jakoby, B. S. Richards, U. W. Paetzold, I. A. Howard and U. Lemmer, "Triple cation mixed-halide perovskites for tunable lasers," *Optics Materials Express,* vol. 7, no. 11, pp. 4082-4094, 2017.

[86] T. C.-J. Yang, P. Fiala, Q. Jeangros and C. Ballif, "High-Bandgap Perovskite Materials for Multijunction Solar Cells," *Joule,* vol. 2, p. 1421–1436, 2018.

[87] D. T. Grant, K. R. Catchpole, K. J. Weber and T. P. White, "Design guidelines for perovskite/silicon 2-terminal tandem solar cells: an optical study," *Optics Express,* vol. 24, no. 21, pp. 1454-1470, 2016.

543

544